Biosorption of Azo Dyes by Raspberry-Like Fe$_3$O$_4$@Yeast Magnetic Microspheres and Their Efficient Regeneration Using Heterogeneous Fenton-like Catalytic Processes over an Up-Flow Packed Reactor

Rui Song [a], Bo Bai*[,b], Gianluca Li Puma [c], Honglun Wang [b], Yourui Suo [b]

[a] College of Environmental Science and Engineering, Chang'an University, Xi'an, 710054, P.R. China;

[b] Northwest Plateau Institute of Biology, Chinese Academy of Sciences, Xining, 810001, People's Republic of China;

[c] Environmental Nanocatalysis and Photoreaction Engineering, Department of Chemical Engineering, Loughborough University, Loughborough, LE11 3TU, United Kingdom.

* Corresponding author: Tel: +86 298 233 9052; Fax: +86 298 233 9961; Email: baibo@chd.edu.cn

Abstract

Raspberry-like Fe_3O_4@yeast composite microspheres, whose properties integrate the biosorption features of yeast cells with the excellent magnetic and catalytic properties of Fe_3O_4 nanoparticles were synthesized by a simple electrostatic-interaction-driven self-assembly heterocoagulation. They were successfully applied in an up-flow packed column for the removal of the model water contaminant methylene blue dye (MB) by consecutive bioadsorption-heterogeneous Fenton oxidation cycles. The as-synthesized Fe_3O_4@yeast composites were characterized by field emission scanning electron microscopy (FE-SEM), energy-dispersive spectroscopy (EDS), powder X-ray diffraction (XRD) and Fourier transform infrared (FT-IR) spectroscopy. The adsorption process was controlled by the electrostatic interactions between the adsorbent and contaminant. The adsorbent is suitable for the adsorption of positively charged compounds at mildly acidic pH, neutral and alkaline pH, with the highest performance observed at alkaline pH. The experimental breakthrough curves measured at different influent MB concentration, flow rate, bed height and pH were modeled by the Yoon-Nelson model. The in-situ regeneration of the contaminant-loaded Fe_3O_4@yeast microspheres and their reuse in multiple cycles was demonstrated by triggering the heterogeneous Fenton-like reaction catalyzed by the supported magnetite. The raspberry-like Fe_3O_4@yeast magnetic microsphere should be a promising and practical adsorbent for removal and destruction of positively charged organic compounds in wastewater.

Keywords: Yeast; Iron oxide; Fixed-bed; Fenton-like reaction; Regeneration; Wastewater

1. Introduction

Organic azo dyes represent more than half of all colouring compounds used by the world textile industry. It has been estimated that 15% of this is released into the environment without an appropriate treatment [1]. Organic azo dyes in wastewater have been classified as priority pollutants particularly owing to the toxicity of their microbial metabolites, which can be mutagenic, genotoxic and carcinogenic [2]. Traditional physico-chemical treatment techniques such as absorption, oxidization, and flotation are usually ineffective to treat low azo dyes concentrations [3]. Biological materials such as micro-organisms (including bacteria, fungi, and algae) [4] and biomass can remove a broad range of azo dyes [5-6]. However, an efficient and sustainable method for pollution abatement that uses biosorbents requires the regeneration and reuse of the sorbent, the destruction of the sorbed/desorbed pollutants, and the safe disposal of the sorbent to the environment. Yeast is an effective biosorbent [7] which meets several green requirements for large-scale pollutant removal including, high selectivity, efficiency, cost-effectiveness, availability and biocompatibility.

Heterogeneous Fenton processes are powerful method for the destruction of azo dyes in aqueous solutions [8–10], especially, those catalyzed by nano-sized magnetite (Fe_3O_4) particles [11-13]. In this system, the octahedral site of the magnetite structure can easily accommodate both Fe^{2+} and Fe^{3+}, allowing the Fe species to be reversibly oxidized and reduced producing •OH radicals when in the presence of H_2O_2 [14-15]. Furthermore, Fe_3O_4 nanoparticles can be easily separated from the reaction system by a simple magnetic separation procedure.

The treatment of contaminated streams by Fenton oxidation with slurry suspensions of Iron oxide can be inefficient since uses large volumes of reagents/catalyst, the water matrix can inefficiently consume •OH radicals and large contact times are often required. In contrast, the efficiency of the

heterogeneous Fenton process for the treatment of wastewater can be increased significantly by applying an enrichment or pre-concentration sorption method prior to the oxidation of the contaminants by the Fenton process on immobilized magnetite.

The combination of an inorganic catalyst with a biological sorbent into hybrid or composite material is attracting increasing attention as it enables new functional properties, which are not possible in their starting components. For example a new class of complex nano-structured hybrid microspheres with a raspberry-like structure can provide a unique micro/nano-environment which has found new applications in the material, chemical, medical and environmental sectors [16-20]. Bai et al. have synthesized novel raspberry-like TiO_2@yeast composites, which were effective photocatalysts for the degradation of dyes [21]. The raspberry-shape provided larger surface area of the supported catalyst. However, such materials required the use of UV light photons, which restrict their technological development.

In this study, we investigate a new composite material, made of raspberry-like Fe_3O_4@yeast microspheres that integrate the biosorption features of yeast cells with the excellent magnetic and catalytic properties of Fe_3O_4 nanoparticles, and its application for the effective removal of contaminants from wastewater by consecutive biosorption and heterogeneous Fenton oxidation/regeneration cycles. In this new material, the traditional magnetic Fe_3O_4 nano-particles were anchored on the yeast surface by an electrostatic self-assembly process that produced a heterogeneous Fenton's catalyst with an unique raspberry-like microstructure. The effectiveness of the raspberry-like Fe_3O_4@yeast composite microspheres for the removal of the cationic dye methylene blue (MB), a model compound used in the standardization of degradation experiments (e.g., ISO 10678:2010), was investigated in a continuous, up-flow, fixed-bed column system. The modeling of the adsorption

phenomena and breakthrough profiles allowed the prediction of the breakthrough time after which the in-situ regeneration of the composite material and the decomposition of MB was triggered through the heterogeneous Fenton reaction catalyzed by the Fe_3O_4 nanoparticles. The robustness of the composite catalytic biosorbent was assessed for multiple adsorption/regeneration cycles.

2. Materials and methods

2.1. Materials

All chemicals used were of analytical grade and used without further purification. The powdered yeast was purchased from Angel Yeast Company. Ferric chloride hexahydrate ($FeCl_3·6H_2O$), absolute ethanol (95 wt %), formaldehyde (CH_2O), hydrazine hydrate ($N_2H_4·H_2O$), methylene blue (MB), and sulfuric acid (H_2SO_4) were provided by Xi'an Chemical Agent Corp. Double deionized water was used throughout all the experiments.

2.2. Preparation of Fe_3O_4@yeast composite microspheres

Fe_3O_4 nanoparticles were firstly synthesized through a hydrothermal method using $FeCl_3·6H_2O$ as a single iron source. Briefly, $FeCl_3·6H_2O$ (1.20 g), CH_2O (2 mL) and $N_2H_4·H_2O$ (5 mL) were dissolved in deionized water (40 mL) under magnetic stirring for 15 min. The solution was then transferred to a Teflon-lined stainless-steel autoclave and heated at 120 °C. After 5 h of reaction, the autoclave was cooled to room temperature. The black Fe_3O_4 nanoparticles were collected magnetically and washed with three consecutive cycles of ethanol and distilled water and then dried in vacuum at 80 °C for 1 h. The dried Fe_3O_4 nanoparticles were then re-dispersed in 150 mL of distilled water and the pH adjusted to 5 by adding H_2SO_4 (1 M). The suspension was stirred for 30 min to promote the de-aggregation of the Fe_3O_4 nanoparticles. In a separate vessel, 1.000 g of yeast powder was washed with distilled water and ethanol three times, respectively. It was dispersed in 150 mL of distilled water and the pH was adjusted to 5 by adding H_2SO_4 (1 M). The suspension was magnetically stirred for 30 min to facilitate

the dispersion of the yeast particles. Finally, the suspensions of Fe_3O_4 nanoparticles and yeast were blended, under continuous stirring for 1 h at room temperature, and then the suspension was left for 3 h without further stirring, during which raspberry-like Fe_3O_4@yeast microspheres were produced via electrostatic self-assembly. The products were collected with a magnet, washed with distilled water and ethanol three times, and then dried at 80 °C for further use.

2.3 Material characterization

The particle size and surface morphology of the samples were observed by a Philips XL 30 field emission scanning electron microscope (FE-SEM). The elemental composition of the composite microspheres was determined with the energy-dispersive spectroscopy (EDS) of the FE-SEM. The crystallographic structures of the samples were identified by powder X-ray diffraction (XRD) using Cu Kα radiation (λ=0.15418 nm) at a scanning rate of $0.02^{°}$/min. Fourier-transform infrared (FT-IR) spectra of samples were recorded on a Bio-Rad FTS135 spectrometer in the range 500-4000 cm^{-1} using a KBr wafer technique, to study the formation and ripening mechanism of the samples.

2.4 Up-flow fixed-bed adsorption experiments

The adsorption and regeneration performance of the Fe_3O_4@yeast composites was investigated in up-flow fixed-bed columns made from glass (12 cm high, 0.8 cm internal diameter) operated in continuous flow. A stock solution of MB (1000 mg/L) was prepared and further diluted to the required feed concentration in each experiment. The effect of the influent concentration (100, 150 and 200 mg/L), flow rate (5, 10, and 15 mL/min), bed depth (1.2, 2.4 and 3.6 cm, corresponding to 0.1, 0.2 and 0.3 g of adsorbent, respectively) and pH (3, 5, 7, 9, 11) on the removal of MB in the columns was investigated. The pH of the dye solutions was adjusted by adding NaOH and H_2SO_4, respectively. Samples collected from the inlet/outlet of the columns at regular intervals were analyzed using a

Jenway 6405 UV−vis spectrophotometer at 664 nm. All of the experiments were performed in triplicate and at room temperature.

2.5 Regeneration experiment

After each adsorption cycle, the exhausted column bed was rinsed by flowing 100 mL double deionized water in the upward direction at the same flow rate used during the adsorption cycle. Then the in-situ regeneration of the Fe_3O_4@yeast bed was triggered by flowing a 10% H_2O_2 aqueous solution through the column bed in the upward direction at a flow rate of 1 mL/min for 1 h. The column was finally rinsed with double deionized water to remove the residual H_2O_2. After the completion of regeneration procedure, the bed was reused for the next adsorption-regeneration cycle, up to three consecutive cycles.

3. Results and discussion

3.1 Characterization and mechanism

Figure 1

Figure 1 shows typical FE-SEM images of the original yeast and the as-obtained Fe_3O_4@yeast composite microspheres under different magnifications. The original yeast (Figure 1(a)) shows cells with a smooth surface and ellipsoidal shape with regular diameter (length 4.0 ± 0.2 μm; width 2.6 ± 0.2 μm). The Fe_3O_4@yeast composite microspheres (Figure 1(b)) maintained the ellipsoidal shape of the original yeast with the rough surface morphology and relatively good monodispersity. The dimensions of the composite microspheres slightly increased (length 4.5 ± 0.2 μm; width 3.0 ± 0.2 μm) suggesting that the Fe_3O_4 nanoparticles (on average 20 nm, inset in Figure 1(c)) were successfully attached onto the surface of yeast. The higher magnification image (Figure 1(c)), shows a rough surface decorated with numerous Fe_3O_4 nanoparticles with exposed yeast bare areas. Furthermore,

each of the composite microspheres approached a distinct raspberry-like morphology.

The EDS analysis of the composite microspheres is shown in Figure S1 of Supporting Information (SI). The C and in part the O peaks resulted from the original yeast cell wall, the Fe and part of the O originated from the Fe_3O_4 supported nanoparticles, and Pt arose from the metal spraying before SEM studies. No other elements were detected, indicating that the final product was impurities free.

Figure 2

Figure 2 shows the XRD patterns of the original yeast, pure Fe_3O_4 nanoparticles and the Fe_3O_4@yeast composite microspheres, respectively. The amorphous yeast showed only a broad peak at around $2\theta = 20^o$ (Figure 2a). The strong and sharp diffraction peaks at 18.4^o, 30.3^o, 35.6^o, 37.3^o, 43.2^o, 53.4^o, 57.2^o and 62.9^o in the patterns of the Fe_3O_4 nanoparticles (Figure 2b) were indexed as (110), (220), (311), (222), (400), (422), (511) and (440) respectively of the face center-cubic phase of Fe_3O_4 (JCPDS card No. 19-0629) which agree with literature [22-23]. The broad peak at $2\theta = 20^o$ of the Fe_3O_4@yeast composite microspheres (Figure 2c) originated mainly by the amorphous structure of yeast. The remaining peaks supported the incorporation of the Fe_3O_4 nanoparticles in the composite and no other diffraction peaks were found in the range investigated indicating the high purity of the products. The intensity of the Fe_3O_4 peaks in the microspheres were lower than those of the pure Fe_3O_4 nanoparticles, which may result from the smaller number of Fe_3O_4 nanoparticles supported on the yeast surface [24, 25] and their good monodispersion surface traits [26,27].

The ferromagnetic properties of the Fe_3O_4@yeast composite microspheres in aqueous solution are shown in Figure S2 (SI). The Fe_3O_4@yeast composite microspheres (40 g/L) were dispersed in deionized water in a cuvette forming a stable suspension (Figure S2 (a)). Under the influence of a magnetic field, there was a rapid separation of the Fe_3O_4@yeast composite particles to the wall of the

cuvette, which yielded an almost colorless aqueous solution (Figure S2 (b) (SI)). This indicated that the Fe_3O_4 nanoparticles were successfully incorporated onto the surface of the yeast hosts endowing the yeast cells with magnetic properties allowing easy separation, recovery and reuse. The black colour imparted by the Fe_3O_4 nanoparticles to the ivory yeast in the composite further supports the successful incorporation of Fe_3O_4 nanoparticles on the yeast surface.

Figure 3

The bonding forces acting between the nanoparticles and the yeast were investigated by FT-IR (Figure 3). The broad and intense peaks in the region from 550 to 650 cm^{-1} of the Fe_3O_4 nanoparticles (Figure 3(a)) are assigned to the Fe-O band. The peaks at around 3300−3700 cm^{-1} and 1384 cm^{-1} belong to OH stretching vibrations and to the H−O−H bending band, suggesting that H_2O molecules adsorbed on the surface of Fe_3O_4 [28]. The additional broad peaks at 3340, 1461, 1360, 1074 and 894 cm^{-1} may result from residual hydrazine hydrate remaining from the synthesis process. Regarding the yeast (Figure 3(b)), the broad and intense peaks at 3292, 2926, 1641, 1384 and 1074 cm^{-1} are assigned to the N−H stretching and bending vibration, the CH_2 asymmetric and symmetric stretching vibration, the amide group, C=O stretching vibration, and the P=O stretching vibration, respectively [29-31]. In the Fe_3O_4@yeast spectra (Figure 3(c)), except for the characteristic absorption peak of yeast, a peak appeared in the range of 550 to 650 cm^{-1}. Moreover, the characteristic peaks of yeast at 3292 cm^{-1}, 1641 cm^{-1} and 1054 cm^{-1} shifted to 3310 cm^{-1}, 1656 cm^{-1}, and 1064 cm^{-1} respectively in the Fe_3O_4@yeast composite microspheres, suggesting that the amino ($–NH_2$), carboxyl (-COO−) and phosphate ($-OPO_3^{2-}$) groups played important roles in the anchoring of the Fe_3O_4 nanoparticles to the yeast surface.

Based on the above analysis, we propose a formation mechanism of Fe_3O_4@yeast composite

microspheres (Figure S4 (a) (SI)). After synthesis of Fe_3O_4 nanoparticles by the hydrothermal route

the attachments of the nanoparticles onto the surface of yeast is driven by the electrostatic-interaction,

self-assembly heterocoagulation between yeast cores and satellite Fe_3O_4 nanoparticles. Specifically, at

the synthesis pH = 5, the Fe_3O_4 nanoparticles are positively charged (pH_{iep} 6.5, [32]) and the yeast is

negatively charged (pH_{iep} 3.0, [33]). Therefore, the opposite zeta-potentials of Fe_3O_4 nanoparticles and

yeast in the range of pH 3.0~6.5 provides a window to assemble them together. The inherent

functional groups in the yeast cell wall, including phosphomannan, mannan, glucan, proteins and

dextran play a significant role in the fabrication of the raspberry-like structure of the composite, since

the abundant hydrophilic anion groups including $-NH-$, $-COO-$, and $-OPO_3^{2-}$ [34, 35] can accumulate

more negative charges on the surface of the yeast [36]. Hereby, the positively charged Fe_3O_4

nanoparticles can spontaneously attach with the negatively charged yeast, and gradually embed onto

the external surface of the yeast, eventually forming the Fe_3O_4@yeast composite microspheres with a

raspberry-like structure.

3.3 Fixed-bed column studies

The partially uncovered yeast surface of the raspberry-like Fe_3O_4@yeast microspheres drives the

adsorption of water contaminants. The yeast surface is usually negatively charged (pH_{iep} 3.3) in

consequence, positively charged water contaminants such as cationic dyes are readily sorbed. To

demonstrate such effect, the sorption of MB from aqueous solution was investigated in a continuous,

up-flow, fixed-bed adsorption/regeneration system. The breakthrough curves were defined by the ratio

of effluent and influent MB concentrations (C_t/C_0) versus time (t). The breakthrough time (t_b, time to

reach 1 mg/L MB in the effluent) and the bed exhaustion time or saturation time (t_e, time to reach

99% of the influent concentration in the effluent) were used to monitor the bed performance. To

analyze the continuous flow, adsorption data included the evaluation of (a) the effluent volume V_{eff}

(mL) (Eq. 1); (b) the total loading of MB to the column q_{tot} (mg) (Eq. 2) at a given flow rate and

influent concentration; (c) the total amount of MB fed to the column m_{tot} (mg) (Eq. 3); (d) the total

percentage removal efficiency φ of MB (Eq. 4); and (e) the equilibrium column loading q_e (mg/g) (Eq.

5).

$$V_{eff}=F \cdot t_e \tag{1}$$

$$q_{tot} = \frac{FA}{1000} = \frac{F}{1000} \int_{t=0}^{t=t_{tot}} C_{ad} dt \tag{2}$$

$$m_{tot} = \frac{C_0 F t_{tot}}{1000} \tag{3}$$

$$\varphi\% = \frac{q_{tot}}{m_{tot}} \times 100 \tag{4}$$

$$q_e = \frac{q_{tot}}{m} \tag{5}$$

Where F is the volumetric flow rate (mL/min), A is the area under the breakthrough curve, C_{ads} (mg/L)

is the adsorbed MB concentration and m is the amount of Fe$_3$O$_4$@yeast in the fixed bed (g),

respectively.

Table 1

3.3.1 Influence of influent dye concentration, flow rate, bed height and mass transfer

Figure 4

The breakthrough curves of MB for an influent dye concentration varying from 100 to 200 mg/L are

shown in figure 4(a). In these experiments, the flow rate, bed height, and pH were kept constant at 5

mL/min, 1.2 cm and 7, respectively. The adsorption data and the parameters are also presented in

Table 1. The observed breakthrough curves followed the typical S-shaped profile. However, a near

linear profile was observed when the influent MB concentration increased to 200 mg/L. The

breakthrough and exhaustion times decreased with increasing influent dye concentration due to the

faster rate of sorbent saturation. When C_0 increased from 100 to 200 mg/L, the equilibrium column

loading (q_e) decreased from 400.5 to 191.1 mg/g (Table 1) which suggests mass transfer limitations.

In consequence, the bed exhaustion is reached before the complete saturation of the adsorbent.

Simultaneously, the percent removal of MB for the tested influent concentrations decreased from

59.3% to 54.6%.

The effect of flow rate (Figure 4(b) and Table 1) was examined by varying it from 5 to 15 mL/min

while C_0, bed height and pH were kept constant at 100 mg/L, 1.2 cm, and 7, respectively. The

breakthrough curves became steeper and shifted towards shorter times as the flow rate increased,

while the breakthrough time and the exhaustion time decreased from 24 to 9 min and from 135 to 35

min, respectively. Furthermore, q_e and φ decreased as the flow rate increased, suggesting a slow

intraparticle adsorption kinetics compared with the column saturation dynamics. Lower flow rates and

longer residence time of MB results in a more efficient diffusion process through the sorbent and

therefore a higher equilibrium column loading.

The effect of bed height on MB removal (Figure 4(c) and Table 1) was investigated at constant flow

rate of 5 mL/min and 100 mg/L influent dye concentration. An increase of the breakthrough time,

exhaustion time and percentage removal, was observed, when the bed height rose from 1.2 to 3.6 cm

(loading of 0.1 to 0.3 g of Fe_3O_4@yeast) which results from the larger sorbent total mass. The

significant reduction in the loading capacity observed with bed height was ascribed to an increase of

pressure drop through the bed, which progressively decreases the rate of intraparticle diffusion.

The equilibrium sorption capacity of the Fe_3O_4@yeast composite microspheres from batch

recirculation experiments at C_0 equal to 100 mg/L and pH 7 was 403.2 mg/g, which suggest that MB

mass transfer was negligible only at $C_0 = 100$ mg/L, $Z = 1.2$ cm and pH $= 7$ (Table 1).

3.3.2 Influence of pH

In these experiments, the pH of MB solution fed to the bed was fixed at 3, 5, 7, 9, and 11, while C_0, flow rate and bed height were kept constant at 100 mg/L, 5 mL/min, and 1.2 cm, respectively. The results (Figure 4(d) and Table 1) show that the adsorption capacity and dye removal rate increased with an increase of pH. Bed exhaustion occurred at 35, 60, 135, 255 and 355 min for pH of 3.0, 5.0, 7.0, 9.0 and 11.0 respectively. This phenomenon is governed by the electrostatic interaction between the dye and the surface charge of the adsorbent [37]. The adsorption of cationic dyes is favored at pH> pH_{iep} (pH_{iep}=isoelectric point, e.g. on $COO-$ groups) and anionic dyes at pH<pH_{iep} (e.g. on Lewis-base–type basal plane sites) [38]. MB is a cationic dye, which exists in solution in the form of positively charged ions. The surface properties of the yeast cores (pH_{iep} = 3.3) and Fe_3O_4 nanoparticles (pH_{iep} = 6.8) are also affected by pH. At pH 3, the surface charge of both yeast and Fe_3O_4 is positive, and thus the abundance of H^+ compete with the cationic MB molecules, reducing the adsorption capacity of the bed causing a rapid breakthrough. At pH 5, the yeast surface has negative and the Fe_3O_4 nanoparticles have positive charge, which increases the adsorption of MB through the surface of the yeast resulting in a longer breakthrough time. At pH 7, 9 and 11, both yeast and Fe_3O_4 have negative charges and the adsorption performance of the bed increases very rapidly has the pH increases. The maximum equilibrium column capacity (1221 mg/g) and MB removal efficiency (63.4%) appear at pH 11, as also reported in other studies with other sorbents [39].

3.4 Mathematical modeling of breakthrough curves

Thomas [40] and Yoon-Nelson [41] models were used to model the experimental breakthrough curves at different influent dye concentration, flow rate, bed height and pH. The linearized form of Thomas' model is widely used to describe column breakthrough data:

$$\ln\left(\frac{C_0}{C_t} - 1\right) = \frac{k_{Th}q_0 m}{F} - k_{Th}C_0 t \tag{6}$$

with C_0 and C_t the influent and effluent dye concentrations (mg/L), k_{Th} the Thomas rate constant

(mL/min·mg), q_0 the equilibrium adsorption capacity (mg/g), m the mass of the adsorbent (g), and F

the solution flow rate (mL/min), respectively. The plots of $\ln[(C_0/C_t) - 1]$ versus time (t) give a straight

line of slope ($-k_{Th}C_0$) and intercept ($k_{Th}q_m m/F$) (figure not shown).

The linearized form of Yoon-Nelson's model is:

$$\ln\left(\frac{C_t}{C_0 - C_t}\right) = k_{YN}t - k_{YN}\tau \tag{7}$$

with the adsorption capacity in the Yoon-Nelson model calculated from [42]:

$$q_{YN} = \frac{q_{tot}}{m} = \frac{C_0 F \tau}{1000m} \tag{8}$$

with, k_{YN} the Yoon-Nelson rate constant (min^{-1}), τ the time required for reaching 50% adsorbate

breakthrough (min) and other parameters as above. The parameters k_{YN} and τ are determined from the

slope and intercept of the linear plots of $\ln[C_t/(C_0-C_t)]$ versus time (t).

Table 2

Table 2 summarizes the model parameters determined from fitting the Thomas and Yoon-Nelson

models to the experimental data. The rate constant (k_{Th}) in Table 2, which characterizes the rate of

solute transfer from the solution to the surface of solid, increased with increasing influent dye

concentration and flow rate and decreased with bed height and pH. These results support an increase

of the importance of mass transfer limitations in the fixed bed as flow rate and dye concentration

decreases and bed height and pH increases. The bed capacity q_0 calculated from Thomas' model

decreased as the dye concentration, flow rate and bed height increased, because of intraparticle

diffusion resistance. The values of k_{YN} increased with an increase in the influent dye concentration

and flow rate, while the corresponding τ values followed an opposite trend. Moreover, the values of

k_{YN} decreased with an increase in both bed height and pH, whereas, a reverse trend was observed for the values of τ.

The theoretical column adsorption capacities calculated from the Thomas and Yoon-Nelson models were compared to the experimental results (Figure S3 (a) (SI)). Here, it was observed that the theoretical column capacity predicted by the Yoon-Nelson model was closer to the experimental data. In addition, the experimental τ values and the theoretical τ values from Yoon-Nelson model were in close agreement (Figure S3 (b) (SI)). Thomas' model neglects external mass transfer and internal diffusion and assumes second-order reversible adsorption kinetics without axial dispersion. Therefore Thomas' model provided a closer fit only for the condition in which mass transfer could be considered negligible (Figure S3 (a) (SI) and Table 1). In contrast, the Yoon–Nelson model is based on the assumption that the rate of decrease in the probability of biosorption for each adsorbate molecule is proportional to the probability of adsorbate adsorption and the probability of adsorbate breakthrough on the biosorbent. The parameters in this model are adjustable and can fit experimental data that may have also been affected by external mass transfer resistances, internal diffusion and axial dispersion. In consequence, the Yoon–Nelson model provided a closer fit of the experimental data within the range of experimental conditions.

3.5 Contaminant oxidation and sorbent regeneration

The magnetic property imparted by the supported Fe_3O_4 on the yeast host is an important functionality. However, a more important functionality is the ability of Fe_3O_4 to trigger the heterogeneous Fenton oxidation reaction, which oxidizes the adsorbed contaminants regenerating the sorbent. The performance of the fixed-bed was evaluated for three consecutive adsorption/regeneration cycles. The influent MB concentration, flow rate, bed height and pH were fixed at 100 mg/L, 5 mL/min, 1.2 cm

and 7, respectively.

Table 3

The column capacity decreased after each regeneration cycle although MB uptake and removal rate remained very high (Table 3). The column bed exhibited equilibrium column loading capacities of over 273.5 mg/g dry beads and removal rate over 57.5% in all three cycles. The reduction in column capacity should be attributed to the inability of the Fenton reaction to remove MB sorbed deeply into the yeast cores, since Fe_3O_4 is primarily supported on the surface. Comparing the parameters q_e and $\varphi\%$ with those reported elsewhere [43-44], the Fe_3O_4@yeast adsorbent presents the advantage that it can be easily regenerated in-situ and reused in multiple cycles.

Figure 5 shows the FT-IR spectra of (a) the synthesized Fe_3O_4@yeast composite, (b) the Fe_3O_4@yeast composite saturated by MB and (c) the saturated composites after Fenton-like reaction.

Figure 5

The spectra of the composite saturated with MB (trace b) displays new band peaks and some obvious red shift peaks in comparison to the fresh composite (trace a). The new bands peaks originated from the MB, particularly those at 1558, 1396, 1051, and 578 cm^{-1} which correspond to the stretching vibrations of the aromatic ring, the C-C and C-S bonds, and the frame vibration of C-S-C [45]. The red shift peaks, such as the bands at 3292 cm^{-1}, 1641 cm^{-1} and 1054 cm^{-1}, suggested the participation of -OH−, -COO−, and $-OPO_3^{2-}$ groups in the adsorption reaction [46]. Notably, the bands associated with MB disappeared after the application of the Fenton-like reaction (trace c).

A schematic of the adsorption and in-situ regeneration mechanisms of the Fe_3O_4@yeast composite microspheres is presented in Figure S4 (b) (SI). The regeneration processes might be attributed to the synergistic effect, which works by integrating the biosorption properties of yeast with the catalytic

16

oxidation properties of the supported Fe_3O_4 nanoparticles. Specifically, the MB molecules are firstly removed from aqueous solution by biosorption and pre-concentrated on the bare areas of the Fe_3O_4@yeast composite microspheres. Then, the enriched MB molecules are decomposed by the Fe_3O_4/H_2O_2 Fenton-like oxidation reaction. The H_2O_2 introduced to the MB saturated column is catalytically decomposed by the supported Fe_3O_4 nanoparticles yielding •OH radicals, which then attack the adsorbed MB molecules regenerating the sorbent. The targeted localized reaction at or in the close proximity of the composite surface is much more efficient than the same Fenton-like reaction carried out by Fe_3O_4 particles in suspensions in slurry reactors. Less catalyst is used, •OH scavenging reactions species in solution are minimized (e.g., carbonates and not targeted species) and also the reaction acts on a much higher pollutant load, which increases the contaminant removal rate (i.e., first-order contaminant removal). In return, the regenerated surfaces of the yeast core can provide continuous adsorption sites for the biosorption of contaminants in repeated cycles.

4. Conclusion

In this study we have investigated a new composite material, which integrates the biosorption features of yeast cells with the magnetic and catalytic properties of Fe_3O_4 nanoparticles, for the effective removal and oxidative destruction of contaminants in water and wastewater. The raspberry-like Fe_3O_4@yeast composite microspheres, were fabricated via a simple electrostatic self-assembly approach using inexpensive and abundant raw materials. These composites exhibited a ferromagnetic property that allows them to be easily separated/recovered by use of an external magnetic field. The adsorption and regeneration performance by a Fenton-like reaction of the microspheres was investigated for the continuous removal of the cationic dye methylene blue (MB) in an up-flow packed column. The adsorption process was controlled by the electrostatic interactions

between the adsorbent and the contaminant. The adsorbent is suitable for the adsorption of positively charged compounds at mildly acidic pH, neutral and alkaline pH, with the highest performance observed at alkaline pH. The raspberry-like Fe_3O_4@yeast composite material can be easily regenerated by applying a Fenton-like reaction and reused. Considering the facile method of fabrication of the composite from abundant and inexpensive raw materials, the easy recovery and separation in water, the superior adsorption performance, the simple and effective way of regeneration and the robustness of the adsorbent for consecutive adsorption/regeneration cycles, we conclude that the raspberry-like Fe_3O_4@yeast magnetic microsphere should be a promising and practical adsorbent for removal and destruction of positively charged organic compounds in wastewater. The embedding of Fe_3O_4 onto the yeast surface can be extended to the simple fabrication of other Fe_3O_4 nanoparticles/bio-macromolecules or other magnetic oxides/yeast materials with similar structure.

Associated Content

Supporting Information

Additional information as noted in the text. This material is available free of charge via the Internet at http://link.springer.com.

References

[1]   R.C. Wu, J.H. Qu, *Water Environ. Res*. **2004**, *76*, 2637-2642.

[2]   P. Kovacic, R. Somanathan, *J. Appl. Toxicol*. **2014**, *34*, 825-834.

[3]   P. Drogui, J.F. Blais, *Recent Patents on Engineering*. **2007**, *1*, 257-272.

[4]   M. Solís, A. Solís, H.I. Pérez, N. Manjarrez, M. Flores, *Process Biochem*. **2012**, 47, 1723-1748.

[5]   V. Janaki, K. Vijayaraghavan, A.K. Ramasamy, K.J. Lee, B.T. Oh, S. Kamala-Kannan, *J. Hazard. Mater*. **2012**, *241-242*, 110-117.

[6]   A.H. Chen, S.M. Chen, *J. Hazard. Mater*. **2009**, *172*, 1111-1121.

[7]   J.X. Yu, R.A. Chi, X.Z. Su, Z.Y. He, Y.F. Qi, Y.F. Zhang, *J. Hazard. Mater*. **2010**, *177*, 222-227.

[8]   M.L. Rache, A.R. García, H.R. Zea, A.M.T. Silva, L.M. Madeira, J.H. Ramírez, *Appl. Catal. B: Environ*. **2014**, *146*, 192-200.

[9]   L. Gu, S. Huang, N. Zhu, D. Zhang, H. Yuan, Z. Lou, *J. Hazard. Mater*. **2013**, *263*, 450-457.

[10] A.D.L. Maria, S. Marta, B. Juan, *React Kinet. Mech. Cat*. **2013**, *110*, 101–117.

[11] X. Liang, Y. Zhong, S. Zhu, J. Zhu, P. Yuan, H. He, J. Zhang, *J. Hazard. Mater*. **2010**, *181*, 112-120.

[12] S. Xavier, R. Gandhimathi, P.V. Nidheesh, S.T. Ramesh, *Desalination and Water Treatment*. DOI:10.1080/19443994.2013.844083.

[13] R.C. Wu, J.H. Qu, *Water Environ. Res*. **2004**, *76*, 2637–2642.

[14] S.H. Kong, R.J. Watts, J. H. *Choi, Chemosphere*. **1998**, *37*, 1473–1482.

[15] B.W. Tyre, R.J. Watts, G.C. Miller, *J. Environ. Qual*. **1991**, *20*, 832–838.

[16] S.J. Guo, S.J. Dong, E.K. Wang, *J. Phys. Chem. C*. **2009**, *113*, 5485–5492.

[17] L. Zhang, Y. Li, J.Q. Sun, J.C. Shen, *Langmuir*. **2008**, *24*, 10851–10857.

[18] H.L. Liu, D. Wang, X.L. Yang, *Colloids Surf. A: Physicochem. Eng. Asp*. **2012**, *397*, 48–58.

[19] X. Wang, T. Akagi, M. Akashi, B. Masanori, *Mini-Rev. Org. Chem*. **2007**, *4*, 51–59.

[20] H.J. Tsai, Y.L. Lee, *Langmuir*. **2007**, *23*, 12687–12692.

[21] B. Bai, N. Quici, Z.Y. Li, G.L. Puma, *Chem. Eng. J*. **2011**, *170*, 451–456.

 [22] S.X. Zhang, X.L. Zhao, H.Y. Niu, Y.L. Shi, Y.Q. Cai, G.B. Jiang, *J. Hazard. Mater*. **2009**, *167*, 560−566.

[23] T. Zhu, J.S. Chen, X.W. Lou (David), *J. Phys. Chem. C*. **2011**, *115*, 9814–9820.

[24] L.F. Duan, S.S. Jia, Y.J. Wang, J. Chen, L.J. Zhao, *J Mater. Sci*. **2009**, *44*, 4407–4412.

[25] N.S. Kim, J.D. Kim, *J. Ind. Eng. Chem*. **2012**, *18*, 1721–1729.

[26] X.D. Su, J.Z. Zhao, Y.L. Li, Y.C. Zhu, X.K. Ma, F. Sun, Z.C. Wang, *Colloids Surf. A: Physicochem. Eng. Asp.* **2009**, *349*, 151–155.

[27] M.S. Hassan, T. Amna, O.B. Yang, H.C. Kim, M.S. Khil, *Ceram. Int*. **2012**, *38*, 5925–5930.

[28] Z.P. Li, L. Gao, S. Zheng, *Appl. Catal. A: Gen*. **2002**, *236*, 163–171.

[29] S. Kumar, T. Surendar, B. Kumar, A. Baruah, V. Shanker, *J. Phys. Chem. C*. **2013**, *117*, 26135−26143.

[30] J.J. Cui, W. He, H.T. Liu, S.J. Liao, Y.Z. Yue, *Colloids Surf. B*. **2009**, *74*, 274–278.

[31] K.C. Blakeslee, A. Robert, S.R. Condrate, *J. Am. Ceram. Soc*. **1971**, *54*, 559–563.

[32] S.J. Joris, C.H. Amberg, *J. Phys. Chem*. **1971**, *75*, 3172–3178.

[33] Y.C. Chang, D.H. Chen, *J. Colloid Interf. Sci*. **2005**, *283*, 446–451.

[34] M. Mercier-Bonin, K. Ouazzani, P. Schmitz, S. Lorthois, *J. Colloid Interf. Sci*. 2004, 271, 342–350.

[35] J.L. Wang, C. Chen, *Biotechnol. Adv*. **2009**, *27*, 195–226.

[36] S. Mann, D.D. Archibald, J.M. Didymus, T. Douglas, B.R. Heywood, F.C. Meldrum, N.J. Reeves, *Science*. **1993**, *261*, 1286–1292.

[37] L.H. Ai, H.Y. Huang, Z.L. Chen, Wei, X.; Jiang, J. *Chem. Eng. J.* **2010**, *156*, 243–249.

[38] M.A.M. Salleh, D.K. Mahmoud, W.A.W.A. Karim, A. Idris, *Desalination*. **2011**, *280*, 1–13.

[39] M. Doğan, M. Alkan, *Chemosphere*. **2003**, *50*, 517-528.

[40] H.C. Thomas, *J. Am. Chem. Soc*. **1944**, *66*, 1664–1666.

[41] Y.H. Yoon, J.H. Nelson, *Am. Ind. Hyg. Assoc. J*. **1984**, *45*, 509-516.

[42] S.H. Hasan, D. Ranjan, M. Talat, *J. Hazard. Mater*. **2010**, *181*, 1134-1142.

[43] D. Kavitha, C. Namasivayam, *Bioresour. Technol*. **2007**, *98*, 14–21.

[44] L. Chen, B. Bai, *Ind. Eng. Chem. Res*. **2013**, *52*, 15568–15577.

[45] L.H. Ai, C.Y. Zhang, F. Liao, Y. Wang, M. Li, L.Y. Meng, J. Jiang, *J. Hazard. Mater*. **2011**, *198*, 282– 290.

[46] S.V. Mohan, S.K. Mohan, M.J. Kathikeyan, *J. Sci. Ind. Res*. **2001**, *60*, 410– 415.

Figure captions

Figure1. FE-SEM images of (a) the originalyeast, (b and c) Fe_3O_4@yeast microspheres observed under different magnifications.

Figure 2.XRD patterns of (a) the original yeast,(b) Fe_3O_4 nanoparticles, and (c)Fe_3O_4@yeast compositemicrospheres.

Figure 3.FT-IR spectrum of (a) the Fe_3O_4 NPs, (b) the pristine of yeast and (c) Fe_3O_4@yeast composite microspheres.

Figure 4. The breakthrough curves for MB adsorption by Fe_3O_4@yeast composites (a) at different influent dye concentration (flow rate = 5 mL/min, bed height =1.2 cm, and pH = 7.0), (b) at different flow rate (influent dye concentration = 100 mg/L, bed height =1.2 cm, and pH = 7.0), (c) at different bed height (influent dye concentration = 100 mg/L,flow rate = 5 mL/min, and pH = 7.0) and (d) at different pH (influent dye concentration = 100 mg/L, flow rate = 5 mL/min, and bed height =1.2 cm).

Figure 5. FT-IR spectra of (a) Fe_3O_4@yeast composites, (b) the Fe_3O_4@yeast composites saturated by MB and (c) the saturated composites after Fenton-like reaction.
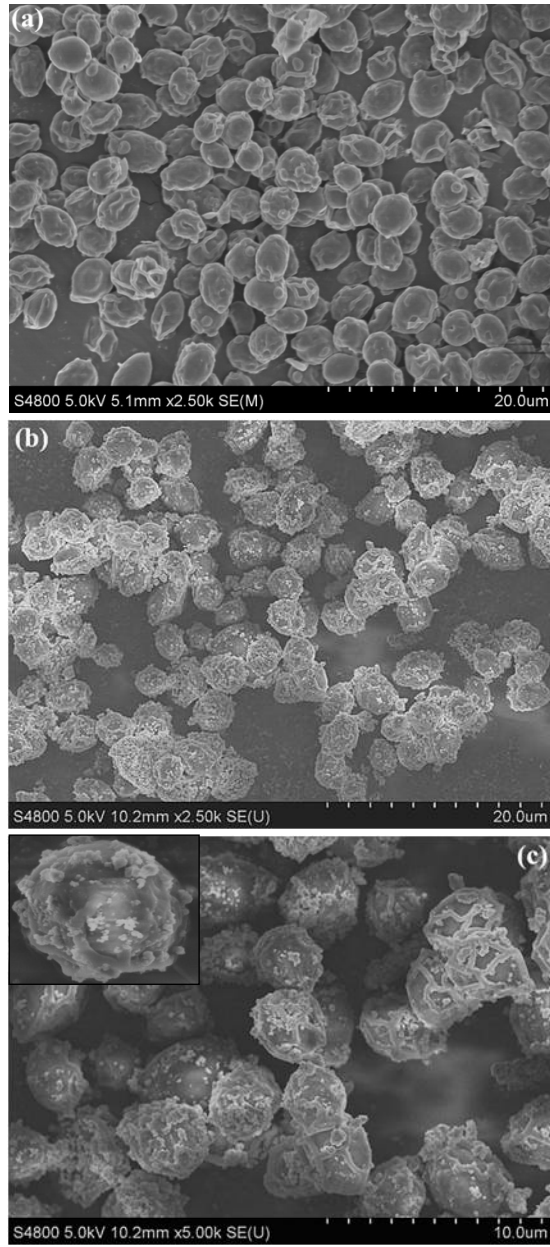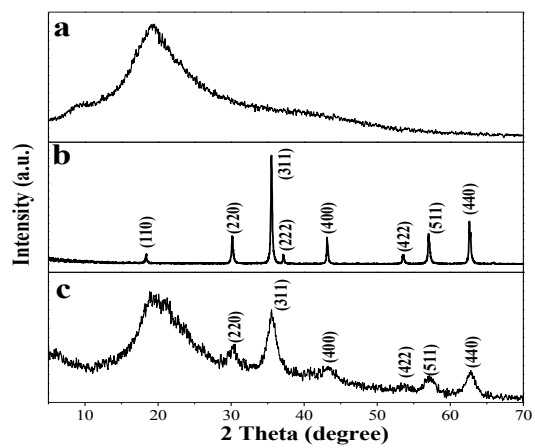
Figure 1.

S4800 5.0kV 5.1mm x2.50k SE(M)   20.0um

S4800 5.0kV 10.2mm x2.50k SE(U)   20.0um

S4800 5.0kV 10.2mm x5.00k SE(U)   10.0um

Figure 2.

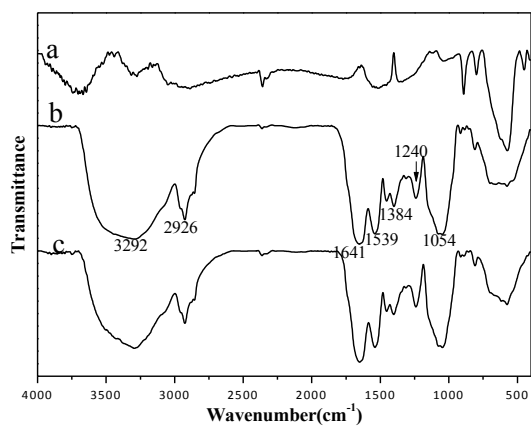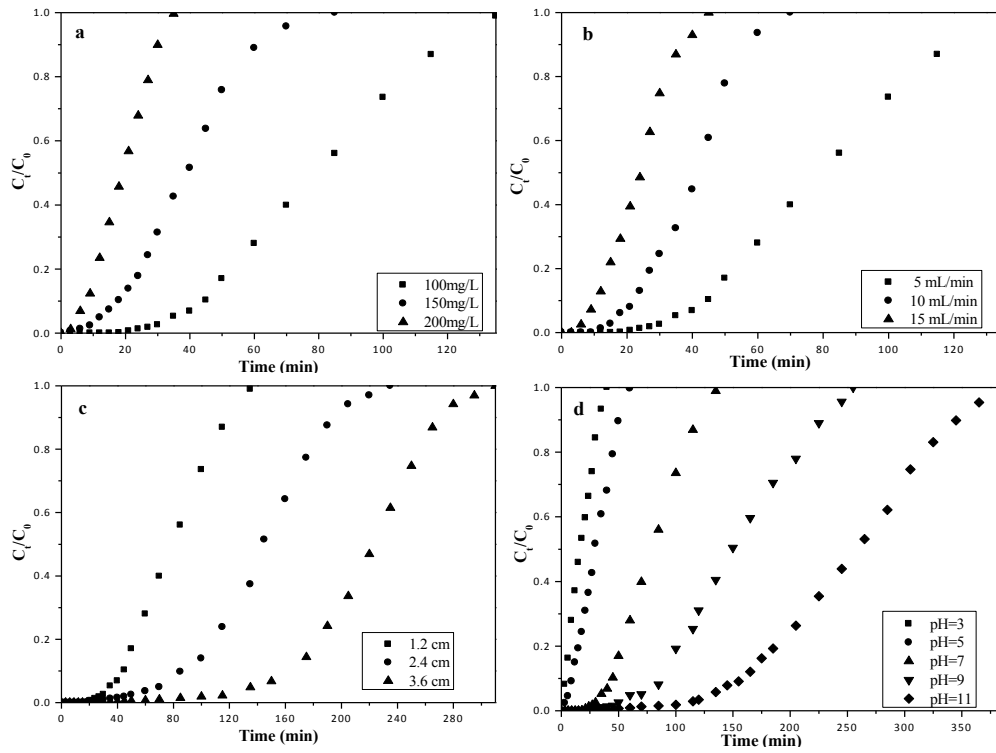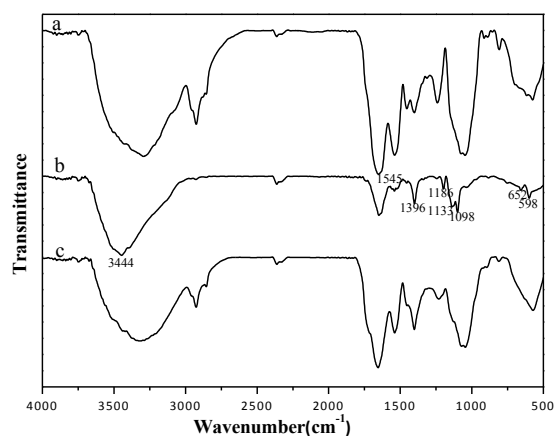**Figure 3.**

Figure 4.

Figure 5.

Table captions

Table 1. Column data and parameters obtained at different conditions.

Table 2. Parameters predicted from the Thomas and Yoon-Nelson models.

Table 3. Column data and parameters obtained after Fenton-like regeneration.

Table 1.

Process parameters	t_b(min)	t_e(min)	V_{eff}(mL)	q_{tot} (mg)	m_{tot} (mg)	Dye removal $\varphi\%$	q_e(mg/g)
Initial dye concentration, C_0(mg/L) (F = 5mL/min, Z = 1.2 cm, pH = 7.0)							
100	24	135	675	40.1	67.5	59.3	400.5
150	6	70	350	29.4	52.5	56.0	294.0
200	3	35	175	19.1	35.0	54.6	191.1
Flow rate,F(mL/min) (C_0 = 100 mg/L, Z = 1.2 cm, pH = 7.0)							
5	24	135	675	40.1	67.5	59.3	400.5
10	18	85	650	35.5	65.0	54.6	355.0
15	9	35	630	31. 1	63.0	49.3	310.9
Bed height, Z(cm) (C_0 = 100 mg/L, F=5 mL/min, pH = 7.0)							
1.2	24	135	675	40.1	67.5	59.3	400.5
2.4	85	235	1175	74.2	117.5	63.1	370.8
3.6	150	310	1550	108.8	155.0	70.2	362.8
pH (C_0 = 100 mg/L, F =5 mL/min, Z = 1.2 cm)							
3	6	40	200	9.9	20.0	49.5	99.0
5	12	60	300	15.2	30.0	50.5	151.5
7	24	135	675	40.0	67.5	59.3	400.5
9	35	255	1275	78.0	127.5	61.2	780.1
11	70	385	1925	122.1	192.5	63.4	1221.0

Table 2.

Parameters	Thomas model			Yoon-Nelson model		
	k_{Th} (mL/min·mg)	q_0(mg/g)	R^2	$k_{YN}\times10^{-3}$ (min^{-1})	τ(min)	R^2
Initial dye concentration (mg/L)						
100	7.29	396.3	0.97	72.9	79.2	0.97
150	8.68	254.2	0.98	130.2	33.9	0.98
200	12.49	153.8	0.90	249.7	15.3	0.90
Flow rate (mL/min)						
5	7.29	396.3	0.97	72.9	79.2	0.97
10	13.44	382.4	0.98	134.4	38.2	0.98
15	17.36	359.9	0.98	173.6	23.9	0.98
Bed height (cm)						
1.2	7.29	396.3	0.97	72.9	79.2	0.97
2.4	4.10	365.4	0.99	49.2	131.7	0.99
3.6	3.38	357.5	0.98	33.8	214.5	0.98
pH						
3	14.01	88.2	0.97	140.1	17.6	0.97
5	11.10	152.8	0.96	111.0	30.5	0.96
7	7.29	396.3	0.97	72.9	79.2	0.97
9	3.86	754.5	0.98	38.6	150.8	0.98
11	2.42	1265.3	0.99	24.2	253.1	0.99

Table 3.

Cycle time	t_b	t_e	V_{eff}(mL)	q_{tot}(mg)	m_{tot}(mg)	Dye removalφ%	q_e(mg/g)
1th	24	135	675	40.1	67.5	59.3	400.5
2th	18	115	500	33.8	57.5	58.7	337.5
3th	12	95	300	27.4	47.5	57.6	273.5

Supporting Information of Figures

Figure S1. EDS spectra of Fe$_3$O$_4$@yeast composite microspheres.

Figure S2. Photographs of the dispersion and separation processes of Fe$_3$O$_4$@yeast: (a) without external magnetic field, and (b) with external magnetic field.

Figure S3. Models fitting of experimental (a) column capacity q (mg/g) and (b) the 50% adsorbate breakthrough time τ (min).

Figure S4. Proposed mechanism of (a) formation and (b) the in situ heterogeneous Fenton-like regeneration of Fe$_3$O$_4$@yeast composites.
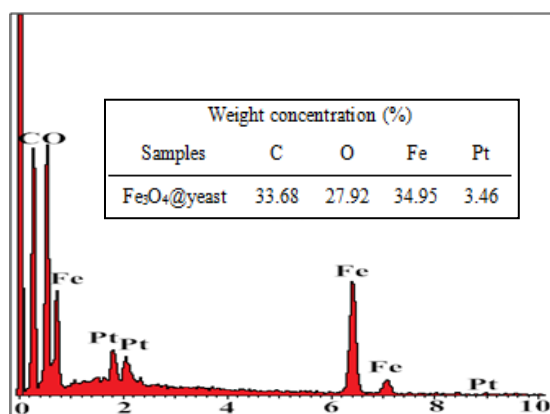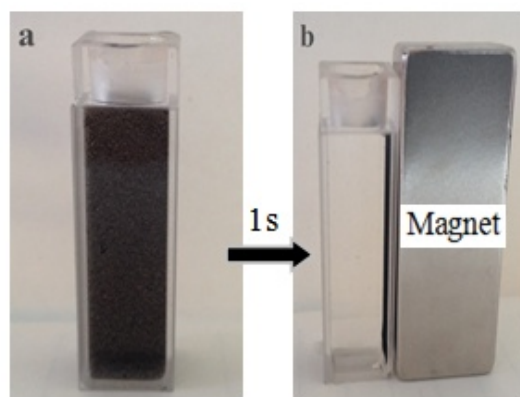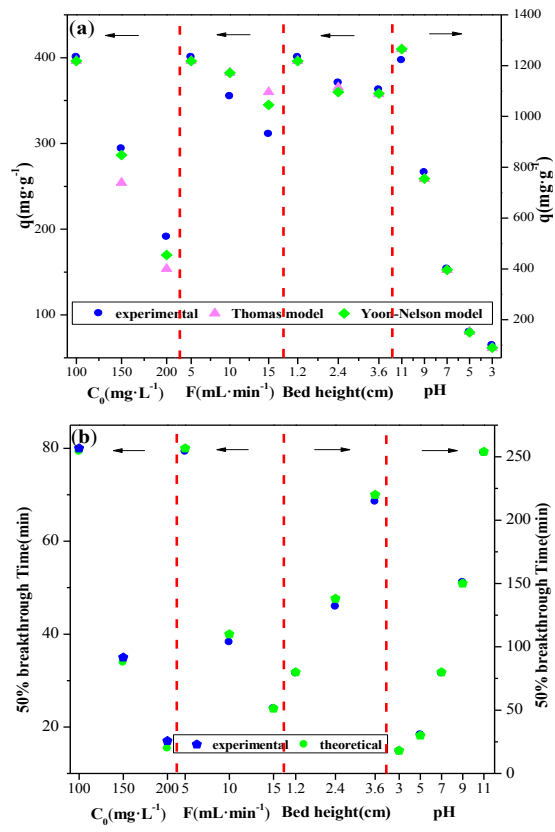
Figure S1.

Figure S2.

Figure S3.

Figure S4.